

Low density nuclear matter with quantum molecular dynamics: The role of the symmetry energy

Rana Nandi* and Stefan Schramm†

*Frankfurt Institute for Advanced Studies,
60438 Frankfurt am Main, Germany*

Abstract

We study the effect of isospin-dependent nuclear forces on the pasta phase in the inner crust of neutron stars. To this end we model the crust within the framework of quantum molecular dynamics (QMD). For maximizing the numerical performance, a newly developed code has been implemented on GPU processors. As a first application of the crust studies we investigate the dependence of the particular pasta phases on the isospin dependence of the interaction, including non-linear terms in this sector of the interactions. Our results indicate that in contrast to earlier studies the phase diagram of the pasta phase is not very sensitive to isospin effects. We show that the extraction of the isospin parameters like asymmetry energy and slope from numerical data is affected by higher-order terms in the asymmetry dependence of the energies per particle. Furthermore, a rapid transition from the pasta to a homogeneous phase is observed even for proton-to-neutron ratios typical for a supernova environment.

* nandi@fias.uni-frankfurt.de

† schramm@fias.uni-frankfurt.de

I. INTRODUCTION

In the crust of neutron stars, at densities well below nuclear saturation density nuclei form crystalline structures embedded in an electron plasma in order to minimize the Coulomb energy. At higher densities, when nuclei are about to dissolve into uniform matter, various interesting spatial structures such as cylindrical and slab shaped nuclei and cylindrical and spherical bubbles etc., collectively called nuclear “pasta”, may appear [1, 2].

The study of the pasta phase is very important for various astrophysical reasons. In core-collapse supernovae the pasta phase significantly affects neutrino transport through the matter, which plays a crucial role in the eventual supernova explosion [3]. On the other hand electron-pasta scattering has a strong impact on the transport properties like electrical and thermal conductivities of the neutron star crustal matter. An enhanced electrical resistivity due to the pasta structures could be a central effect to explain the decay of magnetic field in neutron stars [4] and the thermal conductivity is essential to understand the cooling behaviour of these stars [5, 6]. The presence of the pasta phase might also be important to understand the mechanism of pulsar glitches [7, 8].

So far, a number of authors have studied the properties of the pasta phase. Most of the studies adopt static methods such as liquid-drop models [7, 9], Thomas-Fermi approximations [10, 11] and the Hartree-Fock method [12, 13]. In these models few specific shapes are assumed and free energies are calculated for all the shapes as a function of baryon density. The equilibrium shape at a particular density is then determined by minimizing the free energy. However, to study the formation and evolution of the pasta phase one needs to employ a dynamical approach that allows for arbitrary nuclear shapes and can incorporate the thermal fluctuations on the nucleon distribution in a natural way. Furthermore, as the nuclear matter is a typical frustrated system with competing attractive nuclear and repulsive Coulomb forces, many energetically competing structures might occur. Only a few groups so far have adopted a dynamical approach. The first study in this direction was done by Maruyama *et al* [14], who developed a quantum molecular dynamics (QMD) model to study the pasta phase. Later Watanabe *et al* adopted this QMD model and studied characteristics of the pasta at zero temperature [15] as well as finite temperatures [16] and also the transition between different nuclear shapes [17, 18]. Horowitz *et al* developed a semi-classical dynamic model (SMD) and studied various transport properties [3, 6, 19–22] as well as for-

mation [23] and characteristics [24] of the pasta phase. Recently, Dorso *et al* [25, 26] and Schütrumpf *et al* [27] studied the pasta phase using classical molecular dynamics (CMD) and a time-dependent Hartree-Fock approach, respectively.

The nuclear symmetry energy and its density dependence play crucial roles in both nuclear physics and astrophysics [28, 29]. Laboratory experiments constrain the symmetry energy at saturation density quite well around 30 ± 4 MeV, but its slope L at saturation is still very uncertain and is expected to lie in the range $20 - 120$ MeV [30]. The effect of different L on the pasta phase of inner crust matter of neutron stars has been studied within the liquid drop model [31] as well as the Thomas-Fermi approximation [32–34]. In all of these calculations it was found that the width of the pasta phase decreases with increasing value of L . Sonoda *et al* [35] used two different QMD models with different L to study the pasta phase with proton fraction $Y_p = 0.3$ and found behaviour similar to the static calculations. But to understand the dependence of the pasta phase on the asymmetry dependence of the matter alone, one has to do such a study consistently within the same nuclear model approach. Therefore, in this article we study the dependence of the pasta phase on the asymmetry properties within a single QMD model. The article is structured in the following way. After outlining the general formalism in Sec. II, we present a careful parameter study of different strengths of the isospin forces in Sec. III. Finally, in Sec. IV we draw conclusions and present an outlook of upcoming work in this direction.

II. FORMALISM

In QMD the state of a nucleon is represented by a Gaussian wave packet given as (we set $\hbar = c = 1$)

$$\psi(\mathbf{r}_i) = \frac{1}{(2\pi C_W)^{3/4}} \exp \left[-\frac{(\mathbf{r}_i - \mathbf{R}_i)^2}{4C_W} + i \mathbf{r} \cdot \mathbf{P}_i \right], \quad (1)$$

where \mathbf{R}_i and \mathbf{P}_i denote the center of the position and momentum of the wave packet i , respectively, with the corresponding width C_W . Then the total wave function for the N -nucleon system is obtained by taking the direct product of single-nucleon wave functions

$$\Psi(\{\mathbf{r}\}) = \prod_i^N \psi(\mathbf{r}_i) \quad (2)$$

Here we adopt an effective interaction developed by Maruyama *et al.* [14], to simulate the nuclear matter at sub-saturation densities. The Hamiltonian of the interaction has several

terms:

$$\mathcal{H} = T + V_{\text{Pauli}} + V_{\text{Skyrme}} + V_{\text{sym}} + V_{\text{MD}} + V_{\text{Coul}}, \quad (3)$$

where T is the kinetic energy and V_{Pauli} is the phenomenological Pauli potential which effectively mimics the Pauli exclusion principle. V_{Skyrme} is the nucleon-nucleon potential similar to Skyrme-like interactions, V_{sym} is the isospin-dependent potential related to the symmetry energy, and V_{MD} represents the momentum-dependent potential that arise from the Fock terms of Yukawa-type interactions. Finally, V_{Coul} is the Coulomb potential. The explicit expressions for all the terms are as follows

$$T = \sum_{i,j(\neq i)} \frac{\mathbf{P}_i^2}{2m_i}, \quad (4)$$

$$V_{\text{Pauli}} = \frac{C_P}{2} \left(\frac{1}{q_0 p_0} \right)^3 \sum_{i,j(\neq i)} \exp \left[-\frac{(\mathbf{R}_i - \mathbf{R}_j)^2}{2q_0^2} - \frac{(\mathbf{P}_i - \mathbf{P}_j)^2}{2p_0^2} \right] \delta_{\tau_i \tau_j} \delta_{\sigma_i \sigma_j}, \quad (5)$$

$$V_{\text{Skyrme}} = \frac{\alpha}{2\rho_0} \sum_{i,j(\neq i)} \rho_{ij} + \frac{\beta}{(1+\tau)\rho_0^\tau} \sum_i \left[\sum_{j(\neq i)} \tilde{\rho}_{ij} \right]^\tau, \quad (6)$$

$$V_{\text{sym}} = \frac{C_s^{(1)}}{2\rho_0} \sum_{i,j(\neq i)} (1 - 2|\tau_i - \tau_j|) \rho_{ij} + \frac{C_s^{(2)}}{(1+\gamma)\rho_0^\gamma} \sum_i \left[\sum_{j(\neq i)} (1 - 2|\tau_i - \tau_j|) \bar{\rho}_{ij} \right]^\gamma, \quad (7)$$

$$V_{\text{MD}} = \frac{C_{\text{ex}}^{(1)}}{2\rho_0} \sum_{i,j(\neq i)} \frac{1}{1 + \left[\frac{\mathbf{P}_i - \mathbf{P}_j}{\mu_1} \right]^2} \rho_{ij} + \frac{C_{\text{ex}}^{(2)}}{2\rho_0} \sum_{i,j(\neq i)} \frac{1}{1 + \left[\frac{\mathbf{P}_i - \mathbf{P}_j}{\mu_2} \right]^2} \rho_{ij}, \quad (8)$$

$$V_{\text{Coul}} = \frac{e^2}{2} \sum_{i,j(\neq i)} \left(\tau_i + \frac{1}{2} \right) \left(\tau_j + \frac{1}{2} \right) \iint d^3\mathbf{r} d^3\mathbf{r}' \frac{1}{|\mathbf{r} - \mathbf{r}'|} \rho_i(\mathbf{r}) \rho_j(\mathbf{r}'), \quad (9)$$

where σ_i and τ_i (1/2 for protons and $-1/2$ for neutrons) are the nucleon spin and isospin, respectively and ρ_{ij} , $\tilde{\rho}_{ij}$ and $\bar{\rho}_{ij}$ represent the overlap between single-nucleon densities and defined as

$$\rho_{ij} \equiv \int d^3\mathbf{r} \rho_i(\mathbf{r}) \rho_j(\mathbf{r}), \quad \tilde{\rho}_{ij} \equiv \int d^3\mathbf{r} \tilde{\rho}_i(\mathbf{r}) \tilde{\rho}_j(\mathbf{r}), \quad \bar{\rho}_{ij} \equiv \int d^3\mathbf{r} \bar{\rho}_i(\mathbf{r}) \bar{\rho}_j(\mathbf{r}), \quad (10)$$

whereas the single-nucleon densities are given by

$$\rho_i(\mathbf{r}) = |\psi_i(\mathbf{r})|^2 = \frac{1}{(2\pi C_W)^{3/2}} \exp \left[-\frac{(\mathbf{r} - \mathbf{R}_i)^2}{2C_W} \right], \quad (11)$$

$$\tilde{\rho}_i(\mathbf{r}) = \frac{1}{(2\pi \tilde{C}_W)^{3/2}} \exp \left[-\frac{(\mathbf{r} - \mathbf{R}_i)^2}{2\tilde{C}_W} \right], \quad (12)$$

$$\bar{\rho}_i(\mathbf{r}) = \frac{1}{(2\pi \bar{C}_W)^{3/2}} \exp \left[-\frac{(\mathbf{r} - \mathbf{R}_i)^2}{2\bar{C}_W} \right], \quad (13)$$

TABLE I. Parameter set for the interaction [14]

| | |
|-----------------------------|---------|
| C_P (MeV) | 207 |
| p_0 (MeV/ c) | 120 |
| q_0 (fm) | 1.644 |
| α (MeV) | -92.86 |
| β (MeV) | 169.28 |
| τ | 1.33333 |
| $C_{\text{ex}}^{(1)}$ (MeV) | -258.54 |
| $C_{\text{ex}}^{(2)}$ (MeV) | 375.6 |
| μ_1 (fm $^{-1}$) | 2.35 |
| μ_2 (fm $^{-1}$) | 0.4 |
| C_W (fm 2) | 2.1 |

TABLE II. Symmetry energy coefficients

| Set | $C_s^{(1)}$ (MeV) | $C_s^{(2)}$ (MeV) | γ | $e_{\text{sym}}(\rho_0)$ (MeV) | L (MeV) |
|-----|-------------------|-------------------|----------|--------------------------------|-----------|
| I | 30.0 | -15.0 | 3.0 | 34.6 | 76.8 |
| II | 25.0 | 0.0 | 0.0 | 34.3 | 91.8 |
| III | 18.0 | 22.5 | 3.0 | 34.2 | 114.4 |

with

$$\tilde{C}_W = \frac{1}{2}(1 + \tau)^{1/\tau} C_W \quad \text{and} \quad \bar{C}_W = \frac{1}{2}(1 + \gamma)^{1/\gamma} C_W . \quad (14)$$

The modified widths \tilde{C}_W and \bar{C}_W of the Gaussian wave packet are introduced to adjust the effect of density-dependent terms (for more details see Ref. [14]). In the original model of Maruyama *et al.* [14] there was only the linear term in V_{sym} . To study the density dependence of the symmetry energy we have added a second non-linear term analogously to the density-dependent term appearing in the isospin-0 Skyrme potential V_{Skyrme} . Out of the 13 parameters (Table I and II) of the model 10 are obtained from the properties of nuclear matter at saturation. The Gaussian width C_W is chosen to get a good fit to the binding energies of finite nuclei. The symmetry energy coefficients $C_s^{(1)}$ and $C_s^{(2)}$ are free parameters and are adjusted to achieve reasonable values of the symmetry energy and its slope (L) at saturation (see later discussion).

In order to obtain the equilibrium configuration we use following equations of motion with damping terms [14]:

$$\begin{aligned}\dot{\mathbf{R}}_i &= \frac{\partial H}{\partial \mathbf{P}_i} - \mu_R \frac{\partial H}{\partial \mathbf{R}_i}, \\ \dot{\mathbf{P}}_i &= -\frac{\partial H}{\partial \mathbf{R}_i} - \mu_P \frac{\partial H}{\partial \mathbf{P}_i},\end{aligned}\tag{15}$$

where μ_R and μ_P are damping coefficients, which are positive definite and relate to the relaxation time scale.

III. RESULTS

A. Simulation procedure

Adopting the theoretical framework outlined in Sec. II we have carried out QMD simulation of a system containing neutrons, protons and electrons at essentially zero temperature. The particles are confined in a cubic box, the size of which is determined from a given particle number (\mathcal{N}) and the average density (ρ_{av}). To simulate infinite nuclear matter we impose periodic boundary conditions. We include 2048 nucleons, out of which 608 are protons and 1440 are neutrons, such that the proton fraction (Y_p) is close to 0.3, a value relevant for studies of core-collapse supernovae. We also simulate symmetric nuclear matter with an equal number of protons and neutrons ($Y_p = 0.5$). The number of protons (neutrons) with spin-up are taken to be equal to that of protons (neutrons) with spin-down. To calculate the Coulomb interaction we employ the Ewald method [15], where electrons are considered to form a uniform background and make the system charge neutral.

As an initial configuration we distribute nucleons randomly in phase space. Then with the help of the Nosé-Hoover thermostat [16] we equilibrate the system at $T = 20$ MeV for about 2000 fm/c. To achieve the ground state configuration we then slowly cool down the system in accordance with the damped equations of motion (Eqs. 15) until the temperature reaches a value below 1 keV.

For speeding up the simulation we ported the QMD code to a GPU version, making full use of the nearly 3600 cores in the AMD FirePro S10000 graphics processor unit. With this implementation we can reach the ground state, which requires $\sim 10^4$ fm/c, within a few hrs of computational time. All the simulations are done at the LOEWE-CSC CPU/GPU

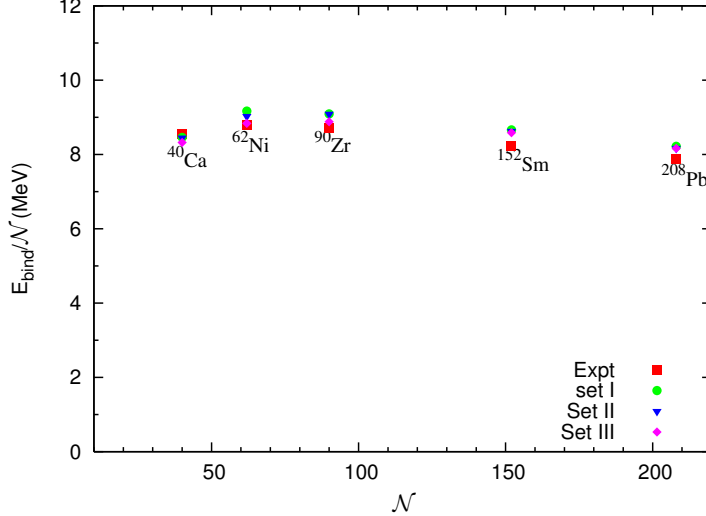


FIG. 1. Binding energies for nuclei obtained from simulation for three different parameter sets: (I) $C_s^{(1)} = 30.0$, $C_s^{(2)} = -15.0$; (II) $C_s^{(1)} = 25.0$, $C_s^{(2)} = 0.0$; (III) $C_s^{(1)} = 18.0$, $C_s^{(2)} = 22.5$. Experimental values are denoted by solid squares.

cluster at Frankfurt University.

B. Finite nuclei and asymmetric nuclear matter

We have chosen three different parameter sets corresponding to three different sets of values for the coefficients $C_s^{(1)}$ and $C_s^{(2)}$ (see Table II). In order to check the validity of our parameter sets, in Fig. 1, we show the binding energies of the ground state of a number of nuclei, covering a range of nuclear masses from Ca to Pb, obtained from our simulation using all three parameter sets. Given the realistically achievable accuracy within a molecular dynamics approach, all of them match the experimental values reasonably well.

Turning to increasingly asymmetric matter, in Fig. 2 the snapshots for the nucleon distributions of various phases for $Y_p = 0.3$ are shown for the parameter set II. It is observed that all the regular pasta shapes i.e. sphere, cylinder, slab, cylindrical hole, spherical hole with increasing density, are reproduced successfully as in the earlier investigation [15]. Similar results are also obtained for other two parameter sets.

In Fig. 3 we plot the asymmetry energy per nucleon which we define as:

$$e_{\text{asym}}(\rho) = e(\rho, Y_p = 0.3) - e(\rho, Y_p = 0.0), \quad (16)$$

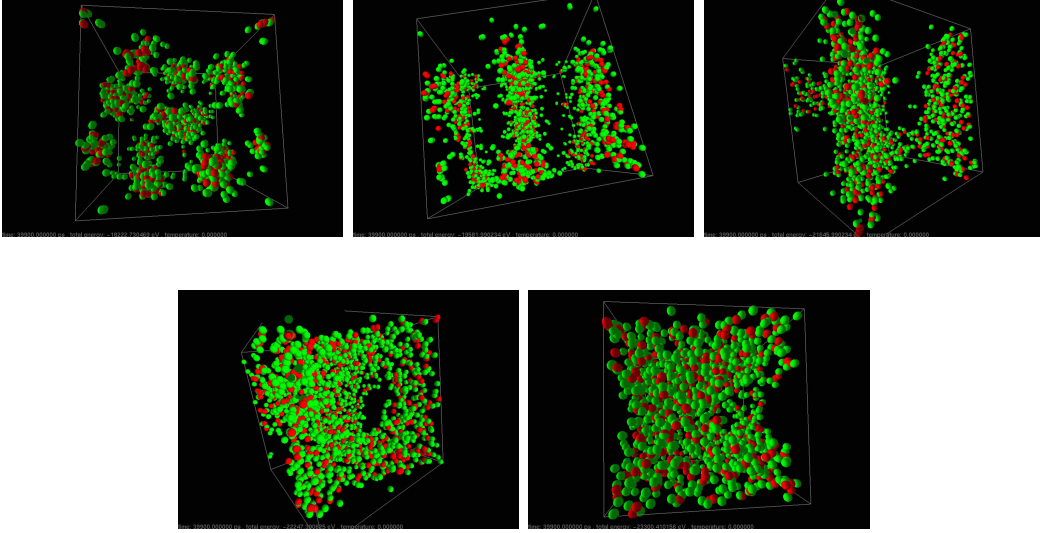


FIG. 2. The nucleon distribution of phases with simple structures of cold matter at $Y_p = 0.3$ and densities (left to right) $0.1 \rho_0$, $0.2 \rho_0$, $0.36 \rho_0$, $0.5 \rho_0$ and $0.575 \rho_0$, respectively. Green (red) spheres represent neutrons (protons).

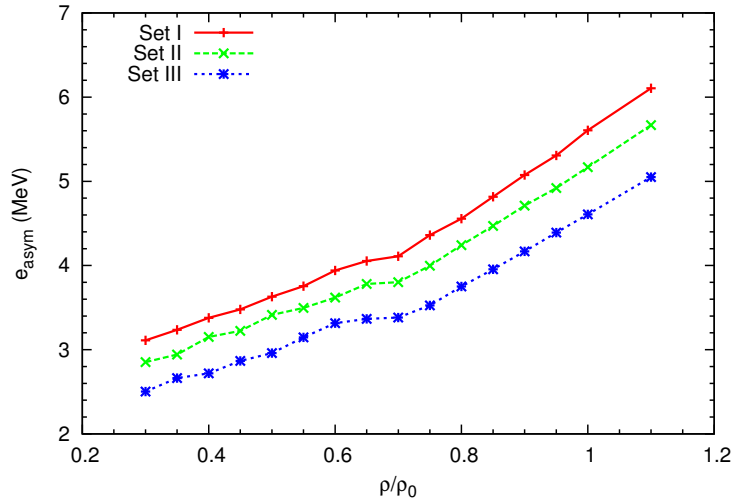


FIG. 3. Asymmetry energy per nucleon obtained from simulation as a function of density for three different parameter sets.

where $e(\rho, Y_p = 0.0)$ is the energy per nucleon for symmetric matter and $e(\rho, Y_p = 0.3)$ is that of matter with $Y_p = 0.3$. The figure shows that three different parameter sets lead to distinctly different asymmetry energies at all densities.

C. Determination of $e_{\text{sym}}(\rho_0)$ and L (parabolic approximation)

Fig. 3 is a direct result from our simulation. To make connection with other analyses of isospin effects we next derive commonly used quantities such as the symmetry energy $e_{\text{sym}}(\rho_0)$ and its slope L at saturation density. The energy per nucleon of asymmetric nuclear matter can be written as a Taylor series with respect to the neutron excess $\delta = (\rho_n - \rho_p)/(\rho_n + \rho_p)$, where ρ_n and ρ_p are the neutron and proton densities, respectively. A commonly used approach retains only the lowest-order non-vanishing term in δ (parabolic approximation):

$$e(\rho, \delta) = e_0(\rho) + e_{\text{sym}}(\rho)\delta^2, \quad (17)$$

where $e_0(\rho) = e(\rho, \delta = 0)$ is the energy per nucleon of symmetric matter and $e_{\text{sym}}(\rho)$ is the nuclear symmetry energy. The symmetry energy can then be expanded (to lowest order) around the normal nuclear density ρ_0 as

$$e_{\text{sym}}(\rho) = e_{\text{sym}}(\rho_0) + L\chi, \quad (18)$$

where $\chi = (\rho - \rho_0)/3\rho_0$ denotes the deviation from ρ_0 and L is the slope of the symmetry energy at ρ_0 given by

$$L = 3\rho_0 \left. \frac{\partial e_{\text{sym}}(\rho)}{\partial \rho} \right|_{\rho=\rho_0}. \quad (19)$$

To evaluate $e_{\text{sym}}(\rho_0)$ and L we run our simulation for different values of δ (from 0 to 1) keeping the density (ρ_{av}) fixed at ρ_0 and switching off the Coulomb interaction, for all three sets of values of $C_s^{(1)}$ and $C_s^{(2)}$ given in Table II. Then we fit the obtained values of energy per nucleon with Eq. (17) and obtain $e_{\text{sym}}(\rho_0)$ as fit parameter (see Fig. 4). Following the same procedure we also determine $e_{\text{sym}}(0.9\rho_0)$ and $e_{\text{sym}}(1.1\rho_0)$, which are then used to calculate L as

$$L = 3\rho_0 \frac{e_{\text{sym}}(1.1\rho_0) - e_{\text{sym}}(0.9\rho_0)}{1.1\rho_0 - 0.9\rho_0}. \quad (20)$$

In Fig. 4 we plot the energy per nucleon obtained from the simulation as well as from the fitting procedure, as a function of δ for three different densities and for three different sets of parameters $C_s^{(1)}$ and $C_s^{(2)}$. The resulting values of $e_{\text{sym}}(\rho_0)$ and L are given in Table II. From the table one can infer that, although the symmetry energies at saturation density are not very different, we get three different values for its slope namely 77, 92 and 114 MeV, respectively.

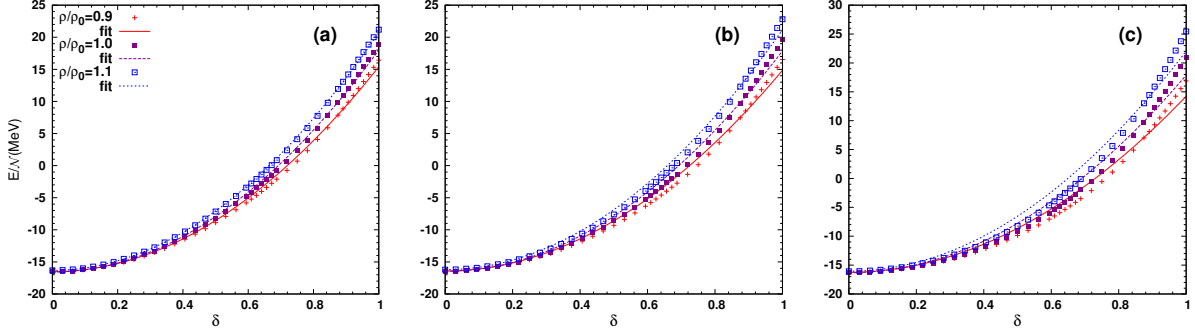


FIG. 4. Fit of energy per nucleon using Eq. (17) for different parameter sets: (a) $C_s^{(1)} = 30.0$, $C_s^{(2)} = -15.0$; (b) $C_s^{(1)} = 25.0$, $C_s^{(2)} = 0.0$; (c) $C_s^{(1)} = 18.0$, $C_s^{(2)} = 22.5$.

D. Minkowski functionals

To quantify various nuclear shapes obtained from the simulations we calculate the corresponding Minkowski functionals [36]. In three dimensions any arbitrary shape can be characterised by four Minkowski functionals: volume V , surface area A , integral mean curvature H and Euler characteristic χ . The last two quantities are determined from the principal curvatures κ_1 and κ_2 on the surface ∂K as

$$H = \frac{1}{2} \int_{\partial K} (\kappa_1 + \kappa_2) dA \quad \chi = \frac{1}{2\pi} \int_{\partial K} \kappa_1 \cdot \kappa_2 dA. \quad (21)$$

The Euler characteristic can also be calculated from the topology of the structure as [36]

$$\chi = \text{number of connected regions} + \text{number of cavities} - \text{number of tunnels}. \quad (22)$$

To calculate the Minkowski functionals we first divide the simulation box in 64^3 voxels and calculate densities at each voxel (j) as $\rho_j^{n,p} = \sum_i^N \rho_i^{n,p}$. We choose a density threshold (ρ_{th}) and turn the density field into a black-and-white data set according to

$$\begin{aligned} \text{voxel } j &= \text{black if } \rho_j \geq \rho_{\text{th}} \\ &= \text{white if } \rho_j < \rho_{\text{th}}. \end{aligned} \quad (23)$$

Then we apply the marching cube algorithm [37] to create a smooth polygonal surface representation of the black voxels. Finally, the Minkowski functionals for the polygon are evaluated with the help of the Karambola package [38]. In order to investigate the dependence of the results on the choice of threshold, we repeat the procedure for a range of

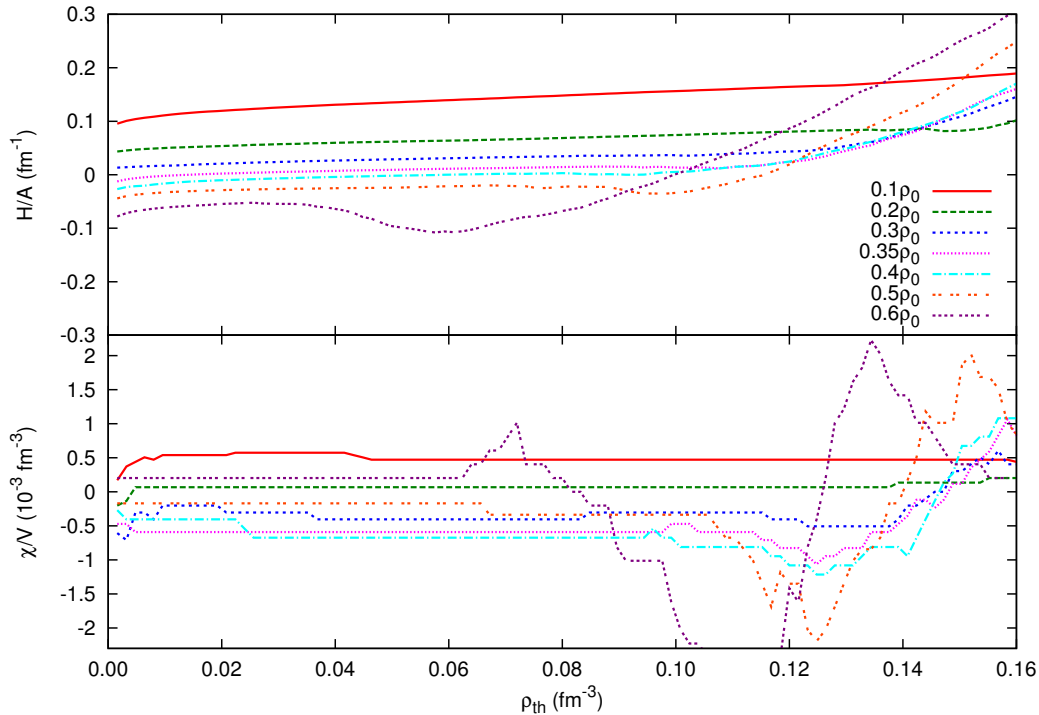


FIG. 5. Normalised mean curvature and Euler characteristic as functions of threshold density for various nucleon densities

densities ρ_{th} . In Fig. 5 we show normalised Minkowski functionals H/A and χ/V for various nucleon densities as functions of the threshold density. One can observe that H/A increases slowly with ρ_{th} , while the slope decreases with increased density. For χ/V , we see that a plateau region exists ($\sim 0.02 - 0.08 \text{fm}^{-3}$) that covers all reasonable values of ρ_{th} . The width of this plateau decreases with density. For our analysis we take the average value across the plateau and evaluate the corresponding standard deviation for obtaining an error estimate.

Next, we compare the Minkowski functionals for three different values of the slope parameter L corresponding to the parameter sets of Table II, at $Y_p = 0.3$. In Fig. 6 we plot normalised mean curvatures as well as the normalised Euler characteristics as functions of normalised density for all three parameter sets. Error bars indicate the standard deviation in the range of ρ_{th} , where χ/V has a plateau (see Fig. 5). From the figure we infer that although there are differences in the detailed behaviour of the Minkowski functionals (especially the Euler characteristics), overall they do not depend much on the parameter sets even if we take the estimated errors into consideration. In terms of L this means that the Minkowski functionals are almost independent of its value. But, this is in contrast to earlier

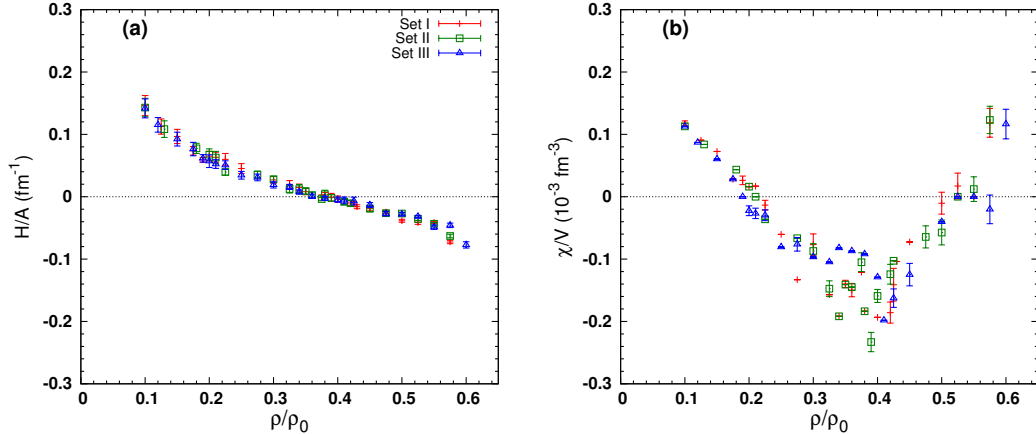


FIG. 6. Comparison of normalised (a) mean curvatures and (b) Euler characteristics as functions of density for different L .

calculations [31–35], where it was found that the lower boundary of the pasta phase gets shifted to higher densities whereas the upper boundary is shifted to lower densities with increasing L . The lower boundary is determined by the fission-like instability that increases with increasing volume fraction of the nuclear region [32]. The volume fraction depends on L through two competing factors. The first important factor is the saturation density, which for the asymmetric nuclear matter (within the parabolic approximation) is given by [32]

$$\frac{\rho_s}{\rho_0} = 1 - \frac{3L}{K_0}\delta^2, \quad (24)$$

where K_0 (280 MeV in our case) is the incompressibility of symmetric nuclear matter. Eq. (24) implies that for asymmetric matter at sub-saturation densities, the average density inside the nuclear region decreases with increasing L , in turn leading to an increased volume fraction. Another controlling factor is the number of dripped neutrons, which increases with increasing L at sub-saturation densities and causes the volume fraction to decrease. If the second factor dominates over the first one, the lower boundary of the pasta phase gets shifted to higher densities. However, for our case the lower boundary lies in the range $0.1 - 0.125 \rho_0$ for all three parameter sets i.e. for all different values of L . The dependence of the lower boundary on L found in Ref. [35] might arise because of the difference in the number of dripped neutrons for the two different models they use. Therefore their result might be caused by adopting different nuclear models in studying the L dependence.

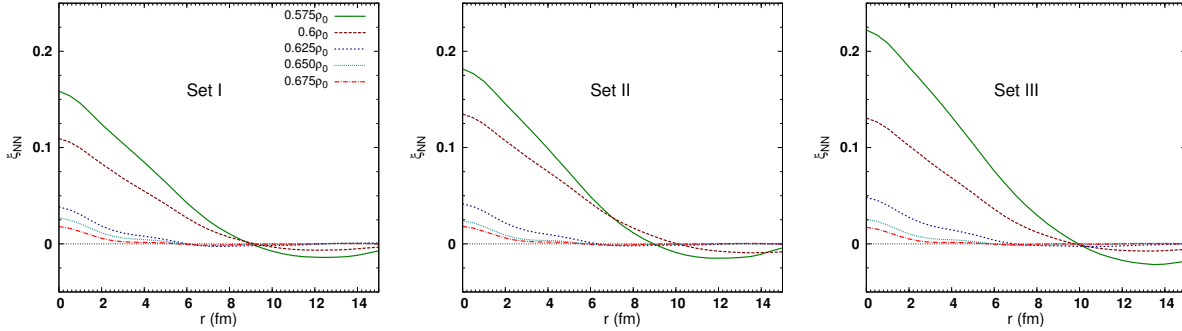


FIG. 7. Two-point correlation function ξ_{NN} of the density fluctuation of nucleons at densities around the transition region of pasta to uniform matter.

E. Transition to uniform matter

The upper boundary, which indicates the transition from pasta phase to uniform nuclear matter, is sensitive to the symmetry energy. The symmetry energy at sub-saturation densities decreases with increasing L (see Eq. (18) and thereby helps the transition to uniform matter to happen at lower densities. To determine the transition density from the pasta phase (spherical bubbles) to uniform matter we calculate the two-point correlation function ξ_{NN} for nucleon density fluctuations defined as:

$$\xi_{NN} = \langle \Delta_N(\mathbf{x}) \Delta_N(\mathbf{x} + \mathbf{r}) \rangle \quad (25)$$

where the average is taken over the position \mathbf{x} and the direction of \mathbf{r} and $\Delta_N(\mathbf{x})$ denotes the fluctuation of the nucleon density field $\rho_N(\mathbf{x})$ defined as

$$\Delta_N = \frac{\rho_N(\mathbf{x}) - \rho_{av}}{\rho_{av}} \quad (26)$$

where $\rho_{av} = \mathcal{N}/V$ is the average density of nucleons. In Fig 7, we plot the correlation function ξ_{NN} in the density range $0.575 - 0.675 \rho_0$. It can be observed that for all three cases long-range correlations vanish between $0.6 \rho_0$ and $0.625 \rho_0$, indicating the transition from pasta to uniform nuclear matter. Moreover, the sudden vanishing of long-range correlations points to the fact that the transition is of first order in nature for $Y_p = 0.3$.

F. Improving on parabolic approximation

Within the parabolic approximation, $e_{\text{asym}}(\rho)$ in Eq. (16) simply equals to $e_{\text{sym}}(\rho)\delta^2$. As the value of $e_{\text{sym}}(\rho_0)$ is almost the same (see Table II) for all three parameter sets, $e_{\text{asym}}(\rho_0)$ also should be equal for all cases for a given δ . But Fig. 3 shows that $e_{\text{asym}}(\rho_0)$ is quite different for different sets of parameter for $\delta \simeq 0.41$. The figure also suggests the parameter set I to have the highest slope and the set III to have the lowest, at ρ_0 . This is just the opposite of the calculated values of L from Eq. (20). This is the result of the parabolic approximation we used for the determination of $e_{\text{sym}}(\rho_0)$ and L for nuclear matter with not such a small asymmetry. It was found from a systematic analytical study of the isospin dependence of the saturation properties of asymmetric nuclear matter that the parabolic approximation is good for $\delta^2 \leq 0.1$ [39]. Furthermore, from Fig. 4 one can observe that the fits to the energy per nucleon are not satisfactory. All these observations lead us to include an additional term in the expansion of the energy per nucleon as

$$e(\rho, \delta) = e_0(\rho) + e_{\text{sym}}(\rho)\delta^2 + e_{\text{sym},4}(\rho)\delta^4, \quad (27)$$

where $e_{\text{sym},4}$ is the fourth-order nuclear symmetry energy [39]. Expanding it around normal nuclear density to lowest order we get

$$e_{\text{sym},4}(\rho) = e_{\text{sym},4}(\rho_0) + L_{\text{sym},4}\chi \quad (28)$$

where $L_{\text{sym},4}$ is the slope parameter of the fourth-order nuclear symmetry energy at ρ_0 given by

$$L_{\text{sym},4} = 3\rho_0 \left. \frac{\partial e_{\text{sym},4}(\rho)}{\partial \rho} \right|_{\rho=\rho_0}. \quad (29)$$

We repeat fitting the data as described earlier but now with Eq. (27). Fig. 8 shows the obtained fits for all three sets. It is evident from the figure that the extended fits are much better, underlining the importance of a careful analysis of the numerical data. The resultant fit parameters are shown in Table III. Similar fits are obtained for two other densities $1.1\rho_0$ and $0.9\rho_0$. Then L is calculated using Eq. (20) and $L_{\text{sym},4}$ as below

$$L_{\text{sym},4} = 3\rho_0 \frac{e_{\text{sym},4}(1.1\rho_0) - e_{\text{sym},4}(0.9\rho_0)}{1.1\rho_0 - 0.9\rho_0}. \quad (30)$$

The resulting values are given in Table III. When we compare Table III with Table II, we see that the value of the symmetry energy $e_{\text{sym}}(\rho_0)$ is no longer fixed around ~ 34 MeV,

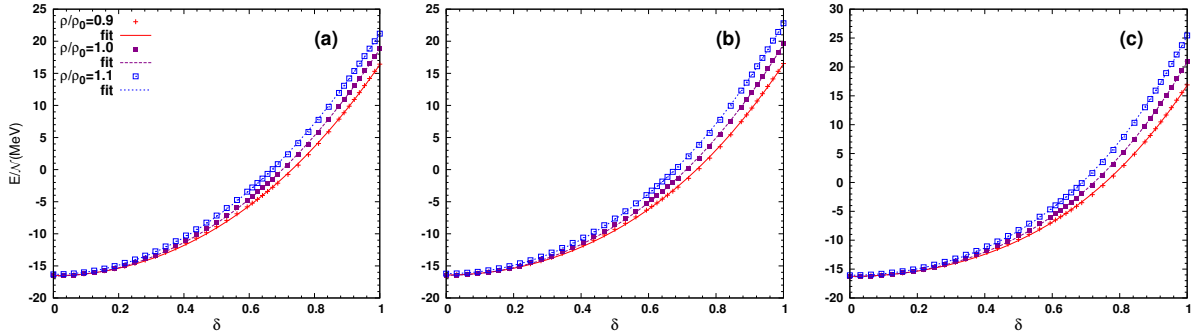


FIG. 8. Fit of the energy per nucleon using Eq. (27) for different parameter sets

TABLE III. Symmetry energy coefficients

| Set | $e_{\text{sym}}(\rho_0)$ (MeV) | $e_{\text{sym},4}(\rho_0)$ (MeV) | L (MeV) | $L_{\text{sym},4}$ (MeV) |
|-----|--------------------------------|----------------------------------|-----------|--------------------------|
| I | 32.1 | 3.27 | 102.2 | -33.2 |
| II | 28.9 | 7.07 | 91.7 | 0.0 |
| III | 24.5 | 12.7 | 76.1 | 50.0 |

but varies in the range $\sim 24.5 - 32.1$ MeV. More interestingly, the values of L are now in opposite order for the same choices of parameters $C_s^{(1)}$ and $C_s^{(2)}$. All these values are now also consistent with Fig. 3. To establish it further we next use these values of L and $L_{\text{sym},4}$ to calculate the saturation densities as [39]

$$\frac{\rho_s}{\rho_0} = 1 - \frac{3L}{K_0}\delta^2 - \frac{3L_{\text{sym},4}}{K_0}\delta^4, \quad (31)$$

For $\delta \simeq 0.41$ we obtain $0.828\rho_0$, $0.832\rho_0$ and $0.861\rho_0$ for Set I, II and III, respectively. These values of saturation densities are very close to the values obtained from our simulation as shown in Fig. 9.

IV. SUMMARY AND CONCLUSIONS

We studied the inner crust of neutron stars within a quantum molecular dynamics approach. Here, in particular we investigated the formation of pasta phases at densities close to the transition to homogeneous matter. The interaction Hamiltonian was based on earlier work by [14], where we extended the isospin-dependent interactions to include non-linear terms in accordance with the isospin symmetric terms. This allowed for a tuning of isospin-

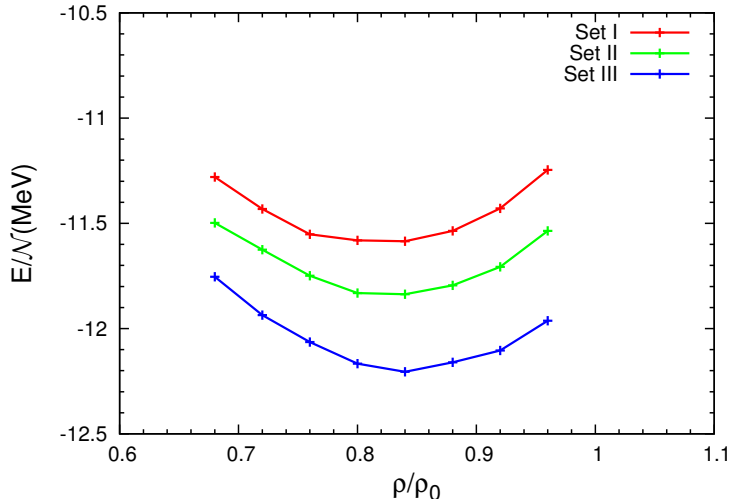


FIG. 9. Energy per particle as function of normalized density for $Y_p = 0.3$ without Coulomb interaction.

related features like the symmetry energy coefficient $e_{\text{sym}}(\rho_0)$ and slope parameter L while staying within the same model approach. We prepared three sets of parameters for the isospin-dependent interaction and obtained very different symmetry energy behaviour. To check the reliability of these parameter sets we calculated the binding energies for the ground state of several nuclei and obtained reasonable agreement with the experimental values for all of them. We derived $e_{\text{sym}}(\rho_0)$ and L for all parameter sets by fitting the numerical data to the expression of energy per nucleon written as Taylor series in neutron excess keeping both the lowest-order term as well as the next higher-order term. The lowest-order approximation, also termed parabolic approximation, led to similar values of $e_{\text{sym}}(\rho_0)$ but different values of L for different parameter sets. On the other hand the higher order approximation produced different values for both $e_{\text{sym}}(\rho_0)$ and L for different sets. Careful investigation of all the simulation data revealed that the higher order term is necessary to have a correct description of the asymmetric nuclear matter with proton fraction typical for supernova environments.

To determine the dependence of the pasta phase on symmetry energy properties we studied the various pasta phases by determining the Minkowski functionals of the simulated nucleon distributions for all parameter sets representing different isospin forces. In contrast to previous molecular dynamics results [35], but in agreement with static model calculations [32], the low-density onset of the pasta phase is quite insensitive to changing isospin asym-

metry properties of the matter. The same holds for the transition density from pasta phase to homogeneous matter where we also have not observed any significant dependence for different isospin behaviour, unlike previous calculations [31–35]. In conclusion, both the low density onset of the pasta and the transition density to uniform matter are not sensitive to $e_{\text{symm}}(\rho_0)$ and L . Furthermore, analysing two-point correlation functions we demonstrated that the transition from the pasta phase to the core is fast, indicating a first-order transition for a proton abundance $Y_p = 0.3$. To see if these conclusions are affected by the finite size effects, as discussed in Ref. [40], we plan to use larger system in future.

The numerical implementation of the simulation was done by making use of GPUs for the most time consuming parts of the calculation. With the computational framework in place, we will expand our simulations of the crust to study its transport properties and extend the simulations to substantially larger systems.

The authors are grateful to the referee for valuable suggestions which greatly improved the article. R. N. acknowledges financial support from the HIC for FAIR project and the NAVI program.

-
- [1] D. G. Ravenhall, C. J. Pethick and J. R. Wilson Phys. Rev. Lett. **50**, 2066 (1983)
 - [2] M. Hashimoto, H. Seki and M. Yamada, Prog. Theor. Phys. **71** 320 (1984)
 - [3] C. J. Horowitz, M. A. Pérez-García and J. Piekarewicz, Phys. Rev. C **69** 045804 (2004)
 - [4] J. A. Pons, D. Viganò and N Rea, Nat. Phys. **9** 431 (2013)
 - [5] W. G. Newton, K. Murphy, J. Hooker and B. A. Li, Astrophys. J. Lett. **779**, L4 (2013)
 - [6] C. J. Horowitz, D. K. Berry, C. M. Briggs, M. E. Caplan, A. Cumming, and A. S. Schneider Phys. Rev. Lett. **114**, 031102 (2015)
 - [7] C. P. Lorenz, D. G. Ravenhall and C. J. Pethick Phys. Rev. Lett. **70**, 379 (1993)
 - [8] G. Watanabe and H. Sonoda, in *Soft Condensed Matter: New Research*, edited by K. I. Dillon (Nova Science, New York, 2007), p.1
 - [9] G. Watanabe, K Iida and K. Sato, Nucl. Phys. A **676**, 455 (2000); **687**, 512 (2001); **726**, 357 (2003)
 - [10] K. Oyamatsu Nucl. Phys. **A561**, 431 (1993)
 - [11] M. Lassaut, H. Flocard, P. Bonche, P. H. Heenen and E Suraud Astron. Astrophys. **183**, L3

- (1987)
- [12] P. Gögelein and H. Müther, *Phys. Rev. C* **76**, 024312 (2007)
 - [13] W. G. Newton and J. R. Stone, *Phys. Rev. C* **79**, 055801 (2009)
 - [14] T. Maruyama, K. Niita, K. Oyamatsu, T. Maruyama, S. Chiba and A. Iwamoto, *Phys. Rev. C* **57**, 655 (1998).
 - [15] G. Watanabe, K. Sato, K. Yasuoka and T. Ebisuzaki, *Phys. Rev. C* **68**, 035806 (2003)
 - [16] G. Watanabe, K. Sato, K. Yasuoka and T. Ebisuzaki, *Phys. Rev. C* **69**, 055805 (2004)
 - [17] G. Watanabe, T. Maruyama, K. Sato, K. Yasuoka and T. Ebisuzaki *Phys. Rev. Lett.* **94**, 031101(2005)
 - [18] G. Watanabe, H. Sonoda, T. Maruyama and K. Sato *Phys. Rev. Lett.* **103**, 121101(2009)
 - [19] C. J. Horowitz, M. A. Pérez-García, D. K. Berry and J. Piekarewicz, *Phys. Rev. C* **72**, 035801 (2005)
 - [20] C. J. Horowitz and D. K. Berry, *Phys. Rev. C* **78**, 035806 (2008)
 - [21] C. J. Horowitz and K. Kadau, *Phys. Rev. Lett.* **102**, 191102 (2009)
 - [22] A. I. Chugonob and C. J. Horowitz, *Mon. Not. R. Astron. Soc.* **407**, L54 (2010)
 - [23] A. S. Schneider, C. J. Horowitz, J. Hughto and D. K. Berry, *Phys. Rev. C* **88**, 065807 (2013)
 - [24] A. S. Schneider, D. K. Berry, C. M. Briggs, M. E. Caplan and C. J. Horowitz *Phys. Rev. C* **90**, 055805 (2014)
 - [25] C. O. Dorso, P. A. Giménez Molinelli and J.A. López, *Phys. Rev. C* **86**, 055805 (2012)
 - [26] P. A. Giménez Molinelli, J. I. Nichols, J. A. Lopez and C. O. Dorso, *Nucl. Phys. A* **923**, 31 (2014)
 - [27] B. Schuetrumpf, M. A. Klatt, K. Iida, J. A. Maruhn, K. Mecke and P. -G. Reinhard *Phys. Rev. C* **87**, 055805 (2013)
 - [28] J. M. Lattimer and M. Prakash, *Phys. Rep.* **442**, 109 (2007)
 - [29] B. A. Li, L. W. Chen and C. M. Ko, *Phys. Rep.* **464**, 113 (2008)
 - [30] Z. Zhang and L. W. Chen *Phys. Lett. B* **726**, 234 (2013)
 - [31] S. S. Bao and H Shen, *Phys. Rev. C* **89**, 045807 (2014)
 - [32] K. Oyamatsu and K. Iida, *Phys. Rev. C* **75**, 015801 (2007)
 - [33] F. Grill, C. Providência and S. S. Avancini, *Phys. Rev. C* **85**, 055808 (2012)
 - [34] S. S. Bao and H. Shen, *Phys. Rev. C* **91**, 015807 (2015)
 - [35] H. Sonoda, G. Watanabe, K. Sato, K. Yasuoka and T. Ebisuzaki *Phys. Rev. C* **77**, 035806

- (2008)
- [36] K. Michielsen and H. De Raedt, Phys. Rep. **347**, 461 (2001)
- [37] W. E. Lorensen and H E Cline, SIGGRAPH Comput. Graph. **21**, 163 (1987)
- [38] G. E. Schröder-Turk *et al.*, New J. Phys. **15** 083028 (2013),
www.theorie1.physik.fau.de/karambola.
- [39] L. W. Chen, B. J. Cai, C. M. Ko, B. A. Li, C. Shen and J. Xu, Phys. Rev. C **80**, 014322
(2009)
- [40] P. A. Giménez Molinelli and C. O. Dorso, Nucl. Phys. A **933**, 306 (2015)